AIAA JOURNAL
Vol. 40, No. 12, December 2002

Stochastic Estimation of Large Structures in an Incompressible Mixing Layer

Michael G. Olsen*
Iowa State University, Ames, Iowa 50011
and
J. Craig Dutton†
University of Illinois at Urbana–Champaign, Urbana, Illinois 60801

High-vector density planar velocity fields were obtained for an incompressible mixing layer using particle image velocimetry (PIV) for the purpose of determining spatial correlations of velocity fluctuations and linear stochastic estimates of the large-scale structures. The linear stochastic estimates were calculated based on the deformation tensor. The velocity ratio of the mixing layer was 0.575, and the density ratio was unity. At the location where the PIV images were obtained, $Re_x = 1.8 \times 10^5$, $Re_{\delta_\omega} = 1.1 \times 10^4$, and the pairing parameter was $Rx/\lambda = 8$. Preliminary hot-film measurements showed the mixing-layer mean velocity and turbulence profiles to be self-similar at this location. The mixing layer was found to be largely two-dimensional with well-organized Brown–Roshko roller structures and braids (Brown, G. L., and Roshko, A., "On Density Effects and Large Structures in Turbulent Mixing Layers," *Journal of Fluid Mechanics*, Vol. 64, 1974, pp. 775–814). Measured velocity fluctuations and Reynolds shear stress data agree well with previous experimental results. The $R_{u'u'}$ correlation is a horizontally oriented ellipse, with a slight inclination from horizontal. The $R_{v'v'}$ correlation is a vertically oriented ellipse. The linear stochastic estimate of a roller suggests that these structures are very slightly elliptical, with a horizontal major axis. The linear stochastic estimate of a braid suggests that the braids are obliquely oriented with stagnation occurring at a point.

Nomenclature

d_p	=	seed particle diameter
d_{pix}	=	camera pixel diameter
d_τ	=	diffraction-limited spot size
$f_\#$	=	focal number
H	=	shape factor
l_c	=	structure spacing
Re_x	=	Reynolds number based on downstream distance
Re_δ	=	Reynolds number based on vorticity thickness
$R_{u'_i u'_j}$	=	spatial correlation of velocity fluctuations
Rx/λ	=	pairing parameter
r	=	velocity ratio, U_2/U_1
s	=	density ratio, ρ_2/ρ_1
U_i	=	freestream velocity of stream I
u_i	=	local velocity
u'_i	=	velocity fluctuation
$\langle u'_i u'_i \rangle$	=	Reynolds stress
x	=	distance downstream from the splitter plate
δ_ω	=	vorticity thickness
δ^*	=	displacement thickness
θ	=	momentum thickness
θ_i	=	momentum thickness of the high-speed boundary layer
μ	=	absolute viscosity
ρ_p	=	seed particle density
τ	=	Stokes number

Introduction

A MIXING layer (or shear layer) is formed by the interaction of two parallel streams of fluid of differing velocity. Mixing layers occur in many problems of engineering importance. The boundary region of a jet, the slip stream behind a wing, and the interface between a recirculation region and a freestream are just a few examples. A typical geometry for a mixing layer is shown in Fig. 1. The subscript 1 is used to denote the properties of the high-speed stream, whereas the subscript 2 denotes the low-speed stream properties.

Ideas concerning the mechanisms of mixing-layer growth and fluid entrainment in turbulent mixing layers have evolved a great deal over the years. In the 1950s and 1960s researchers[1,2] imagined entrainment taking place by a process called "nibbling." In this hypothesis, a wavy interface exists between the turbulent fluid within the mixing layer and the irrotational fluid in the freestreams. This wavy surface advances into the freestream, thus expanding the mixing layer by vorticity diffusion. This nibbling was believed to be uniform over the entire surface, resulting in the experimentally measured linear growth rate of turbulent mixing layers.[3] Flow visualization experiments performed in the early 1970s allowed researchers to expand on this hypothesis for mixing-layer growth.

In their seminal paper on turbulent mixing layers, Brown and Roshko[4] found that mixing-layer growth and fluid entrainment are dominated by large-scale turbulent structures. These large-scale structures resemble spanwise-oriented rollers that convect downstream at a speed approximately equal to the mean of the two freestream velocities. These structures cause the mixing layer to grow through two mechanisms. The first of these involves entrainment of freestream fluid into the roller structures and can be described as "gulping." This process was first described by Roshko[5] and later analyzed in greater detail by Dimotakis.[6] Irrotational freestream fluid is drawn into the roller structures where, because of the large surface area of the interface between the irrotational and rotational fluid, vorticity can rapidly diffuse into the irrotational fluid, thus causing the mixing layer to grow.

A second mechanism for the growth of the mixing layer is the interaction of two or more roller structures to form a single larger structure. This process is best understood if the life-cycle of roller structures is described. The rollers can be formed from instabilities that may exist in the mixing layer both before the transition to turbulence[7,8] and after.[9,10] The initial spacing of the rollers is dependent on the frequency of the most dominant instabilities. This was shown when experimenters could vary the size and shape of the

Received 29 September 2001; revision received 5 February 2002; accepted for publication 10 July 2002.

*Assistant Professor, Department of Mechanical Engineering, 3025 H. M. Black Engineering Building; mgolsen@iastate.edu. Member AIAA.
†Professor, Department of Mechanical and Industrial Engineering, 1206 W. Green Street. Associate Fellow AIAA.

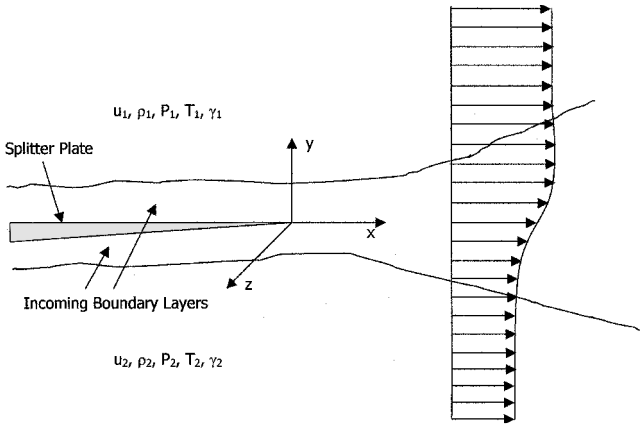

Fig. 1 Schematic of a mixing layer.

rollers by forcing the instabilities at various frequencies.[11] As these structures convect downstream, occasionally two or more structures will combine to form a larger structure.[4,12] This interaction increases both the size of the structures as they convect downstream (thus, increasing the width of the mixing layer) and the spacing between the remaining structures, which is proportional to the distance downstream from the origin. The structure spacing is proportional to the mixing-layer thickness, with

$$l_c = 2.9\delta_\omega \tag{1}$$

as the generally accepted relationship.[4]

Karasso and Mungal[13] were able to predict the downstream location of the first, second, third, etc., pairings, based on a parameter first introduced by Huang and Ho[14] called the pairing parameter. This parameter is defined as Rx/λ, where $R = (1-r)/(1+r)$ and $r = U_2/U_1$ is the velocity ratio. According to Karasso and Mungal,[13] λ can be estimated as $\lambda \approx 30\theta_i$, where θ_i is the momentum thickness of the high-speed boundary layer at separation from the splitter plate. Karasso and Mungal found that, generally, the first roller pairing occurs when $Rx/\lambda = 4$, the second roller pairing occurs when $Rx/\lambda = 8$, the third roller pairing occurs when $Rx/\lambda = 16$, and so on. It was after the third roller pairing that the mixing layer achieved self-similarity in the sense that the roll-off exponent of the power spectra of the velocity fluctuations reached a constant value. The effectiveness of the pairing parameter in characterizing mixing-layer behavior was further demonstrated in the experiments of Meyer et al.[15]

At sufficiently high Reynolds numbers, the mixing layer will develop secondary streamwise vortices in addition to the large-scale spanwise roller structures. These secondary vortices appear as streamwise ribs in the braid region between roller structures[16] and originate from secondary instabilities in the large-scale rollers. These streamwise vortices lead to an increase in mixing as they increase the interfacial area between the rotational fluid within the mixing layer and the irrotational fluid in the freestreams. Breidenthal[17] found that the onset of the formation of these three-dimensional streamwise vortices is delayed as the velocity ratio is increased. Breidenthal also observed that, before this mixing-layer transition, spanwise, sinuous "wiggles" can be observed in the mixing layer. Tung and Kleis[18] observed "kinks" in the large spanwise vortices after the third roller structure pairing, and it was these kinks that eventually developed into streamwise vortices.

Metcalfe et al.[19] performed a direct numerical simulation (DNS) for a temporally evolving mixing layer. The calculations were done on a $64 \times 64 \times 64$ grid and were run over a long enough time to allow two complete vortex pairings to take place. The calculations were performed with and without forcing and confirmed the experimentally verified result that forcing could vary the strength and spacing of the vortices.

Moser and Rogers[20,21] and Rogers and Moser[22] have performed the most ambitious DNS of incompressible mixing layers to date. They used a spectral method consisting of $512 \times 210 \times 192$ Fourier modes to solve for the velocity field of a temporally evolving mixing layer. The calculations were begun by using a previously calculated turbulent boundary-layer velocity field on each side of the mixing layer at time $t = 0$. The simulations were run long enough to allow for three vortex pairings to occur and, thus, provide detailed images of evolving roller structures at various stages. Comparisons of computed Reynolds stresses to experimental data are quite good, suggesting that the computational grid was indeed fine enough to capture all of the scales of turbulence.

Planar velocity measurements in incompressible mixing layers have been attempted in the past. Dimotakis et al.[23] used particle streak velocimetry to measure the velocity field in an incompressible mixing layer, but their technique led to irregularly and sparsely spaced vectors. Post et al.[24] also performed particle tracking experiments, although the usefulness of their measurements is limited due to the high Stokes number (0.2) of the seed particles used. Oakley et al.[25] performed high-speed cinematic particle image velocimetry (PIV) experiments on incompressible mixing layers. Because their velocity fields were correlated in time, their analysis concentrated on the temporal evolution of the large-scale structures in the mixing layer. From their velocity vector fields, they were able to calculate temporal correlations, measure convective velocities of individual structures, and estimate structure lifetimes. For the experiments of Oakley et al., $Re_\delta = 2.6 \times 10^4$. One of their findings was that the velocity field structure differed from previous lower Reynolds number experiments. At their highest Reynolds number, the two-dimensional rollers and braids were replaced by complex three-dimensional structures (a phenomenon known as the mixing transition). The Reynolds number for the present experiment was much lower than that of Oakley et al., and, thus, the current measurements are for a mixing layer that is more two dimensional in nature.

The objective of the present mixing-layer experiments was to obtain high-vector density planar velocity fields using PIV and then calculate spatial correlations of velocity fluctuations and linear stochastic estimates of large-scale structures to further the understanding of the characteristics and behavior of the large-scale structures found within the mixing layer. Linear stochastic estimates were calculated for roller structures and the braid regions between them, providing information on roller structure size, shape, and orientation in a mean sense. Because calculation of the linear stochastic estimates requires differentiation of the spatial correlations, the high spatial resolution of the correlations is necessary to guarantee the accuracy of the linear stochastic estimates.

Experimental Apparatus and Procedure

The flow facility for these experiments is of the blowdown type with high-pressure air supplied by an Ingersoll-Rand compressor, which provides up to 1200 standard cubic feet per minute (SCFM) at an operating pressure of 115 psig (793 kPa). The high-pressure air first flows into several interconnected pressure vessels with a total volume of about 150 m^3. After first passing through a control valve, the air from these vessels enters the test facility stagnation chamber. The flow rate to the test section is regulated by using the pressure in the stagnation chamber as a feedback signal to the control valve, which opens or closes as necessary to keep this pressure constant. During the experiments, the control valve actually did little if any opening or closing. The flow rate was so small that it was only a fraction of the capabilities of the air compressors, and so the tank farm remained at a constant pressure of 115 psig (793 kPa). The control valve was essentially set at a certain position to throttle the flow and stayed at that location throughout the run.

Figure 2 is a schematic of the test section used in the mixing-layer experiments. Separate pipes supply air for the top (high-speed) and bottom (low-speed) streams. The pipe to the bottom stream is fitted with a globe valve to allow for throttling. A combination of three screens and one sheet of honeycomb reduces the freestream turbulence intensities and provides uniform flow to each of the two streams. In each freestream, the flow is accelerated by a converging nozzle with a 6:1 contraction ratio. The two streams come together at the tip of the splitter plate, which has been machined such that it is only a few hundredths of a millimeter thick at its tip with a 3-deg angle between the two streams. The test section is 63.5 mm high $\times$ 102 mm wide, and it is 356 mm in length. Optical access to the test section is available through fused silica windows in all four walls of the facility.

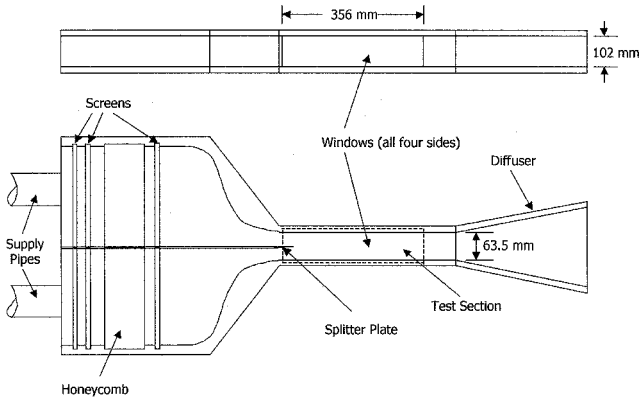

Fig. 2 Mixing-layer facility schematic.

For the PIV measurements, it was necessary to seed the flow with particles. The seed particles must be small enough so that they can accurately follow the sharpest velocity gradients present in the flowfield, but must be large enough that they scatter sufficient light to expose the photographic film used in the PIV experiments. Titanium dioxide particles with an average diameter of 0.4 μm were found to meet both of these criteria.

An analysis of the dynamics of particles in compressible mixing layers was performed by Samimy and Lele,[26] and their results were used to determine the effectiveness of the seed particles used in the present experiments. Samimy and Lele found that the important parameter for measuring tracer particle effectiveness is the Stokes number τ, where $\tau = (\rho_p d_p^2 \Delta U)/(18\mu\delta_\omega)$. For $\tau < 0.05$, the error in velocity measurements due to particle slip is negligible. For the present incompressible mixing layer experiments, $\tau = 0.0036$, and, thus, the titanium dioxide particles should closely follow the flow.

A hot-film anemometry system was used to collect mean velocity and velocity fluctuation data at various locations in the test section. The velocities were measured with a TSI Model 1210-20 hot-film probe interfaced to a TSI IFA-100 flow analyzer. The signal from the flow analyzer was sent to a computer where it was digitized by a National Instruments AT-MIO-16E10 data acquisition board. The velocity data were then recorded and analyzed using National Instruments LabVIEW software.

The particle image velocimeter used in these experiments consists of the acquisition system and the interrogation system. The acquisition system includes the lasers, beam-shaping optics, and 35-mm camera used to obtain the particle image photographs of the flowfield. The interrogation system comprises the charge-coupled device (CCD) camera, light source, positioning system, control computer, and digital signal processors necessary to calculate vector fields from the PIV photographs.

The lasers used in the acquisition system were a pair of Continuum YG681C-10 Nd:YAG lasers. The timing of the acquisition system is controlled by a Stanford Research Systems DG535 digital delay pulse generator. The pulse generator triggers each of the lasers at 4 Hz and allows the user to control the time separation between the firing of the lasers, as well as to coordinate the firing of the lasers with the operation of the camera. A small uncertainty in the time separation in the firing of the two lasers is present due to the pulse jitter of each laser, which is approximately 1 ns. A time separation of 6700 ns was used in these experiments, resulting in an uncertainty of less than $\pm 0.04\%$ due to pulse jitter.

The PIV photographs were obtained using a Canon EOS 35 mm camera fitted with a 100-mm focal-length lens. This lens has a maximum f of 2.8. However, the lens aperture was partially closed for the mixing-layer experiments, resulting in an f of 6.7. Kodak T-Max 100 film was used for all of the PIV photographs.

After the PIV photographs were obtained by the acquisition system, the velocity vector fields were calculated by the interrogation system. The photographic negative is placed in a glass sandwich, and a small region of it is illuminated by a fiber optic white light source that is focused onto a CCD camera. A two-axis positioner controls the position of the negative, allowing different regions of the flowfield recorded on the photographic negative to be imaged. A frame grabber residing within the host computer digitizes the image, and the digitized image is then sent to a digital signal processing (DSP) board. The DSP board performs a cross-correlation analysis on the digitized image to find the velocity vector at each interrogation spot.

In a detailed study of interrogation accuracy, Prasad et al.[27] found that when particle images are well resolved during digitization, the uncertainty of the measurement is roughly equal to one-tenth of the particle image diameter. A particle image is considered to be well resolved when the ratio of the particle image diameter to the size of a CCD pixel when projected back onto a photograph is at least $d_\tau/d_{\text{pix}} = 4$.

For the PIV photographs in the present experiment, the particle diameter is 40 μm (the diffraction-limited spot size), and each 128×128 pixel interrogation spot is 800×800 μm. Thus, $d_{\text{pix}} = 6.25$ μm, and the particle images are well resolved ($d_\tau/d_{\text{pix}} = 6.4$). The measurement uncertainty can, thus, be approximated by one-tenth of the particle diffraction-limited spot size, which is 4 μm. The bottom freestream velocity corresponds to a displacement of 162 μm, and the top freestream velocity corresponds to a displacement of 281 μm. Thus, the experimental uncertainty is 2.5 and 1.4% for the top and bottom streams, respectively.

Experimental Results and Discussion

For these mixing-layer experiments, the high-speed stream was set to 40 m/s, and the low-speed stream was set to 23 m/s, corresponding to a velocity ratio of $r = u_2/u_1 = 0.575$. This velocity ratio was chosen because it corresponds to a mixing layer thick enough that a large number of velocity vectors could be measured across the thickness using PIV, but not so thick that the mixing layer grew into the top and bottom walls of the wind tunnel. These freestream velocities were measured using a pitot-static pressure probe and an oil-column manometer (as well as a hot-film anemometer and PIV). Because both streams are relatively low-speed air at approximately atmospheric conditions, the density ratio is unity, $s = \rho_2/\rho_1 = 1$ (corresponding to a homogeneous mixing layer).

Hot-Film Anemometry Results

Velocity measurements were first obtained with the hot-film anemometer to characterize the incoming top- and bottom-stream boundary layers and also the mixing layer at the PIV measurement location. First, boundary-layer measurements were obtained 15 mm upstream from the tip of the splitter plate in both the top and bottom streams. For each location, the hot-film data consist of an ensemble of 16,384 realizations collected at 10,000 Hz. The data signal was low-pass filtered at 5000 Hz by the signal conditioner in the IFA-100 so that no aliasing occurred.

When the edge of the boundary layer is defined as the location where the mean velocity is 99% of the freestream, the thickness of the top boundary layer is approximately 1.26 mm, and the momentum thickness is 0.16 mm. The displacement thickness δ^* is about 0.39 mm, resulting in a shape factor of $H = \delta^*/\theta = 2.4$. The peak turbulence intensity in the top boundary layer is about 5.5%, and the turbulence intensity of the high-speed (top) stream is less than 0.5%.

The bottom-stream boundary layer is thicker than the top-stream boundary layer. Again, when the edge of the boundary layer is defined as the location where the mean velocity is 99% of the freestream value, the thickness of the lower boundary layer is approximately 3.61 mm, and the momentum thickness is 0.31 mm. The displacement thickness is 0.40 mm, resulting in a shape factor of $H = \delta^*/\theta = 1.3$. The peak turbulence intensity is about 10% in the bottom-stream boundary layer, and the freestream turbulence is about 0.8%.

The question arises as to why the bottom-stream boundary layer is so much thicker than that of the top stream. The authors believe that this is due to two factors. The first factor is that the top boundary layer is transitional, whereas the bottom boundary layer is fully turbulent. The second factor is the finite angle of the splitter plate as it comes to a point at the tip. The top of the splitter plate is flat, but the bottom is inclined at an angle of 3 deg. The bottom stream is,

thus, slightly diverging near the splitter plate tip, causing the bottom boundary layer to grow in a slightly adverse pressure gradient. It, therefore, grows faster than the top boundary layer, which is not subject to a pressure gradient.

In addition to the mean and fluctuating velocity measurements, velocity power spectra were also measured in both the top and bottom freestreams and the top and bottom boundary layers. For the power spectra measurements, the hot-film data consist of 32,768 points collected at 40,000 Hz. The signal was low-pass filtered at 20,000 Hz to eliminate any aliasing effects. An ensemble of 100 spectra was obtained at each location, and these were then averaged. The boundary-layer measurements were obtained 0.5 mm above or below the splitter plate, whereas the freestream measurements were obtained 13 mm from the splitter plate. All of these measurements were obtained 15 mm upstream of the splitter-plate tip. All of the spectra are very smooth, with no indication of any spikes in the spectra that would indicate forcing at a specific frequency due to periodic vortex shedding, or some other forcing, such as acoustical or resonance effects in the facility and the open/shut operations of the control valve.

Finally, hot-film traverses of the mixing layer were made at locations 130, 155, and 180 mm downstream of the tip of the splitter plate to investigate if the mixing layer had achieved self-similarity. As in the boundary-layer traverses, the mixing-layer data at each spatial location consist of an ensemble of 16,384 realizations collected at 10,000 Hz. The data signal was once again low-pass filtered at 5000 Hz to eliminate aliasing. These traverses indicated that the mixing layer had achieved self-similarity in both the mean velocity and turbulence intensity at all locations downstream of $x = 130$ mm.

PIV Results

An ensemble of 111 PIV velocity vector fields was obtained at a location 150 mm downstream of the splitter plate tip. At this location, the Reynolds numbers based on distance from the splitter-plate tip and local mixing-layer vorticity thickness are $Re_x = 1.8 \times 10^5$ and $Re_{\delta_\omega} = 1.1 \times 10^4$, respectively. For this Reynolds number Re_{δ_ω}, the large-scale roller structures present in the mixing layer should be highly two dimensional and coherent; indeed, the PIV results presented herein show this to be the case. As was done by Karasso and Mungal,[13] the momentum thickness of the high-speed boundary layer was used in calculating the pairing parameter, which at this location is computed to be $Rx/\lambda = 8$. Because $Rx/\lambda = 8$ corresponds to the approximate location of the second roller pairing,[13] a great deal of roller–structure interaction can be expected in the PIV velocity vector fields of the current results.

In the velocity vector fields presented here, an interrogation spot size of 0.8 mm on a side was used, and, with 50% overlap between adjacent interrogation spots, this results in a spatial resolution of 0.4 mm in both the x and y directions. Each of these vector fields measured 110 vectors in the x direction and 120 vectors in the y direction (or 44 mm in the x direction by 48 mm in the y direction) for a total of 13,200 vectors, with the vector field centered approximately at the y-direction (transverse) center of the mixing layer.

Instantaneous Velocity Fields

A typical velocity vector field for the incompressible mixing layer is shown in Fig. 3. In this vector field, the large-structure convective velocity of 31.5 m/s (average of the mean freestream velocities) has been subtracted from each of the vectors. This is necessary to visualize the turbulent structures in the mixing layer clearly. Also, in this field, every measured vector has been plotted, resulting in a spatial resolution of 0.4 mm. The velocity field shown in Fig. 3 contains two large Brown–Roshko[4] roller structures, one at $x = 158$ mm and one at $x = 183$ mm, with a braid (or stagnation region) between them at $x = 170$ mm. These two roller structures do not appear to be interacting with each other. As a reminder, the coordinate system used in Fig. 3 is such that the tip of the splitter plate is at the origin (0,0). It can, thus, be seen that because the centers of the roller structures are at approximately $y = -7$ mm, the mixing layer grows toward the low-speed stream, which is the expected result.[3] Also, the vectors in the top freestream are pointed toward the mixing layer

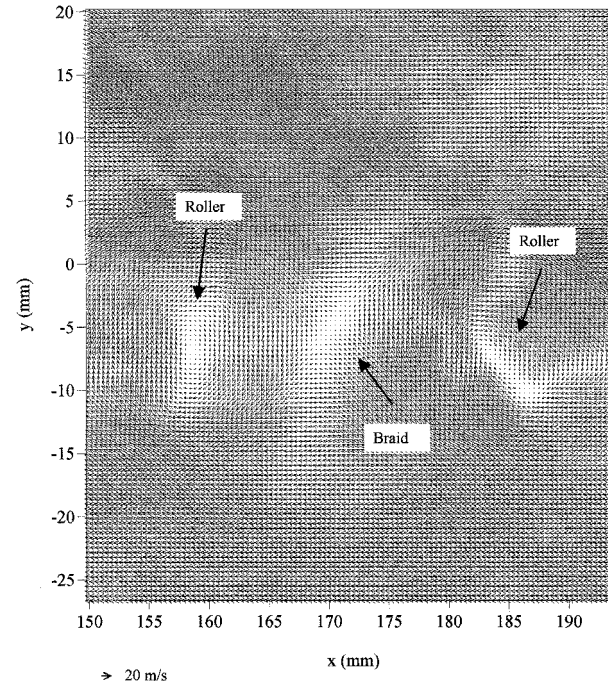

Fig. 3 Typical incompressible mixing-layer velocity vector field; spatial resolution is 0.4 mm (every measured vector shown).

(a characteristic made more pronounced by the subtraction of the convective velocity), showing the entrainment of freestream fluid into the mixing layer. The vectors in the bottom freestream point only slightly toward the mixing layer, suggesting that entrainment of fluid into the mixing layer is greater on the high-speed side than on the low-speed side, another expected result based on previous mixing-layer research.[5]

Figure 3 shows one typical result for these experiments, namely, a vector field with two roller structures and one braid. Another common result in the ensemble is a vector field containing one roller structure and two braids. These two situations make up the vast majority of vector fields in the current ensemble, comprising over 80% of the realizations. This is because the mean spacing of the roller structures at the downstream location where the PIV photographs were obtained makes these flow-structure groupings most likely. In this 80% majority of the vector fields, the large-scale structures are all of nearly the same size and similar spacing.

Mean Velocities and Reynolds Stresses

Although the number of planar velocity fields in the ensemble is relatively small, a method was devised to obtain reliable turbulence statistics from the PIV vector fields. This was done by collapsing each of the 110 columns of velocity vectors in each PIV vector field into a single column and then combining the columns from each of the individual vector fields into a single ensemble. The resulting ensemble was then used to calculate mean velocity and Reynolds stress profiles. Even though the two dimensionality of the planar velocity information was lost, this method increased the size of the ensemble to 12,210 realizations at each transverse y location, resulting in more stable statistical quantities. Although this procedure is justified in the sense that all measurements are made in the self-similar region, it is emphasized that these were not 12,210 independent realizations. In this experiment, neighboring vectors (indeed, vectors in large areas of the flowfield) are obtained from the same large structures and, thus, are not truly independent. Therefore, the statistical profiles presented here are obtained at high data density but are averaged over a relatively limited number (about double the number of images) of large structures. Also, this technique does introduce some error because the mixing layer grows as it moves downstream and, thus, is slightly thicker on the right edge of the vector field than the left. The growth rate is small, however, and, thus, the effect of the growth rate on the mean velocity and Reynolds stress profiles is also small.

Table 1 Comparison of peak turbulence quantities for incompressible mixing-layer experiments

Experiment	Re_x	Re_δ	$\langle u' \rangle / \Delta U$	$\langle v' \rangle / \Delta U$	$\lvert \langle u'v' \rangle / (\Delta U)^2 \rvert$
Present	1.8×10^5	1.1×10^4	0.18	0.16	0.010
Tung[29]	2.0×10^6	4.5×10^4	0.16	0.14	0.011
Spencer[30]	2.6×10^6	——	0.19	——	——
Batt[31]	7.0×10^5	——	0.17	——	——
Wygnanski and Fielder[32]	4.7×10^5	6.0×10^4	0.18	0.15	0.010
Browand and Latigo[33]	1.8×10^6	2.1×10^5	0.16	0.13	0.013
Urban and Mungal[34]	3.2×10^6	1.5×10^5	0.17	0.12	0.011

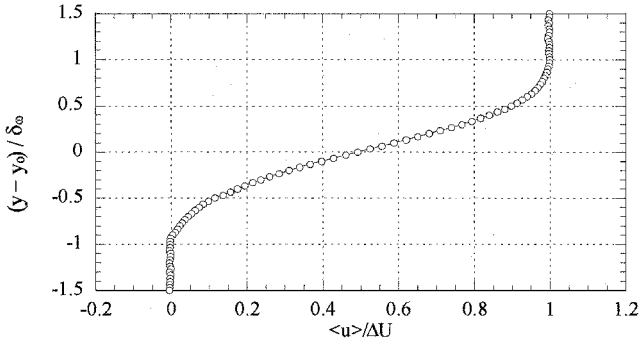

Fig. 4 Mean u-velocity profile as measured by PIV. The solid line represents Görtler's analytical solution.

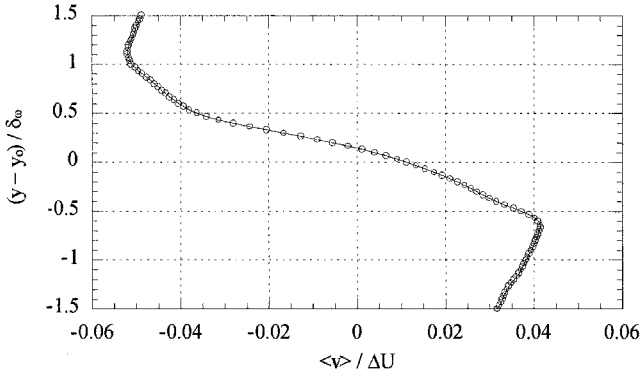

Fig. 5 Mean v-velocity profile as measured by PIV.

The mean u-velocity profile as obtained by PIV is shown in Fig. 4. It has the same error-function shape as predicted by the analytical solution of Görtler (see Ref. 28). (Görtler's analytical solution is depicted by the solid line in Fig. 4.) The y axis has been normalized by the mixing-layer vorticity thickness. This normalization of the transverse coordinate is used in each of the PIV profile plots. The location y_0 is defined as the point where the mean u velocity is equal to the average of the top and bottom freestream velocities.

The mean v-velocity profile is shown in Fig. 5. The mean v velocity is seen to decrease (become more negative) with increasing positive distance from the center of the mixing layer, reaching a peak value at 1.0 mixing-layer thicknesses from the center. Similarly, the mean v velocity increases moving away from the center of the mixing layer toward the low-speed stream, reaching a peak value at 0.6 mixing-layer thicknesses from the center. The peak negative and positive values of the mean v velocity in the top and bottom freestreams, respectively, are indicative of the asymmetric entrainment of fluid into the mixing layer from each of the freestreams.

Reynolds stress profiles, as obtained by PIV, and normalized by $(\Delta U)^2$, are shown in Fig. 6. Both of the Reynolds normal stresses, $\langle u'u' \rangle$ and $\langle v'v' \rangle$, are seen to peak near the center of the mixing layer and decay to smaller values as the observation point moves toward the freestreams. The Reynolds shear stress $\langle u'v' \rangle$ behaves similarly, although its values are negative, as expected. Generally, the turbulence intensities $\langle u' \rangle / \Delta U$ and $\langle v' \rangle / \Delta U$ (square root of the normal stresses) are presented in the literature instead of the dimensionless normal stresses. Peak values of these, as well as the peak Reynolds shear stress, are shown in Table 1, along with results from previous experiments.[29–34] Although there is some variation in the peak stresses found by the various researchers, in each experiment (that measured both) the peak value of $\langle u' \rangle / \Delta U$ was greater that the peak value of $\langle v' \rangle / \Delta U$. This characteristic is also seen in the present PIV results. For the present experiment, the peak value of $\langle v' \rangle / \Delta U$ is slightly higher than in the previous experiments, but the peak value of $\langle u' \rangle / \Delta U$ agrees well with previous measurements. The peak value of $|\langle u'v' \rangle / (\Delta U)^2|$ is also in close agreement with previous work. The result for $\langle v' \rangle / \Delta U$ may merely be a consequence of the facility and Reynolds number used in the present experiment. Indeed, Dziomba and Fiedler[35] determined that even very weak perturbations caused by conditions in the wind tunnel (not forced perturbations) could affect the characteristics of the mixing layer formed. This effect is more pronounced when the incoming boundary layers are turbulent. The relatively low Reynolds number of the current experiment may also result in a more "two-dimensional" turbulence field and better organization of the large structures than for experiments at higher Reynolds numbers.

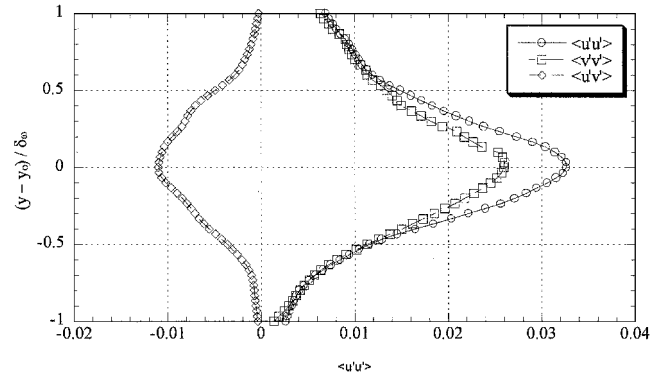

Fig. 6 Reynolds stress profiles as measured by PIV.

Spatial Correlations

The instantaneous nature of the PIV velocity vector fields facilitates the computation of spatial correlations of velocity fluctuations. First, spatial correlations were calculated for six points in each vector field. Each of these basis points was on the transverse centerline of the mixing layer (defined as the location where the mean u velocity is the average of the velocities of the top and bottom freestreams), and the points were spaced evenly in the x direction. For each of the points, the spatial correlation was calculated as

$$\langle u_i'(x, y) u_j'(x, y; X, Y) \rangle = u_i'(x, y) u_j'(x + X, y + Y) \qquad (2)$$

where (x, y) are the coordinates of the basis point and (X, Y) are the displacements from the basis points. For these calculations, the area over which the spatial correlations are calculated is a square of 81×81 vectors centered on the basis points. The ensemble average of the spatial correlations for all of the basis points (666 realizations in all) is then calculated and normalized by $\sqrt{[\langle u_i'^2(x, y) \rangle \langle u_j'^2(x, y) \rangle]}$, resulting in

$$R_{u_i' u_j'}(x, y; X, Y) = \frac{\langle u_i'(x, y) u_j'(x, y; X, Y) \rangle}{\sqrt{\langle u_i'^2(x, y) \rangle \langle u_j'^2(x, y) \rangle}} \qquad (3)$$

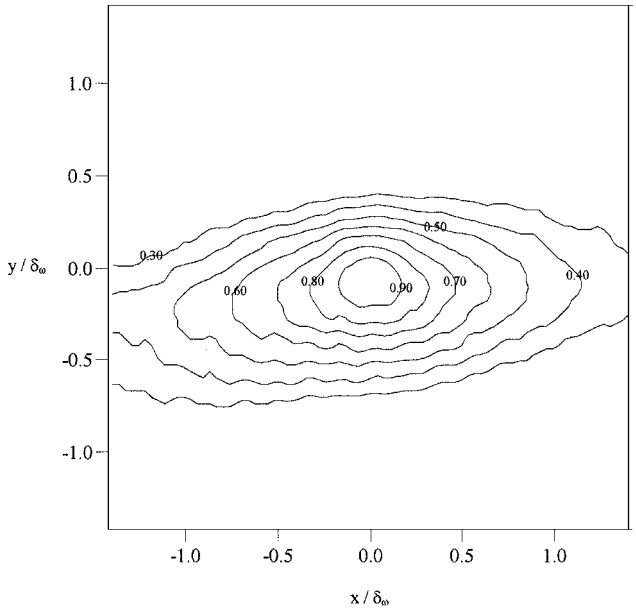

Fig. 7 Spatial correlation $R_{u'u'}$ as measured by PIV.

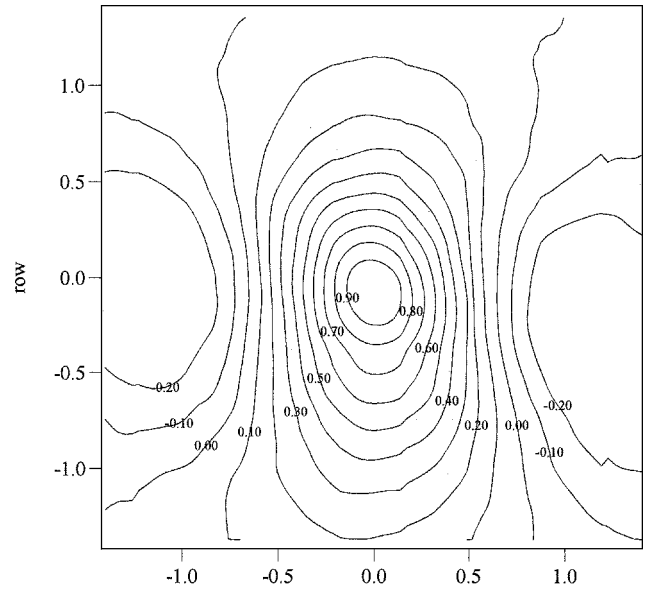

Fig. 8 Spatial correlation $R_{v'v'}$ as measured by PIV.

The spatial correlation $R_{u'u'}$ as measured by PIV is shown in Fig. 7. The correlation field is an ellipse with the major axis inclined at a small angle with respect to the x direction. This shape is expected for a mixing layer dominated by large roller structures and braids. Consider, for example, the instantaneous velocity field shown in Fig. 3. Along the mixing-layer centerline (the line along which the mean u velocity is the average of the two freestreams, which extends from $y = -3.4$ mm on the left edge of the velocity vector field to $y = -4.2$ mm on the right edge), the u velocity varies very slowly because each individual large-scale structure convects downstream with a nearly constant u velocity. The $R_{u'u'}$ correlation, thus, remains high over long distances in the x direction. There is not a corresponding long correlation distance in the y direction, however. Along a line of constant x, there are differing fluctuations around the mean u velocity as the y location is varied. Thus, $R_{u'u'}$ drops off quickly in the y direction.

Measurements of $R_{u'u'}$ by Tung[29] using hot-wire anemometry indicated the same tilted elliptical shape as in Fig. 7. However, the correlation fell off faster with increasing displacement from the basis points in his measurements than in the current PIV measurements. This difference most probably arises from the fact that Tung's measurements were obtained at a higher local Reynolds number, $Re_{\delta_\omega} = 4.7 \times 10^4$, compared to $Re_{\delta_\omega} = 1.1 \times 10^4$ for the PIV measurements. Recall that above $Re_{\delta_\omega} = 2 \times 10^4$, the mixing layer becomes highly three dimensional (mixing transition), and the large-scale structures become less coherent than at lower Reynolds numbers. Because the Reynolds number for Tung's experiment falls far above $Re_{\delta_\omega} = 2 \times 10^4$, the large-scale structures in his experiment are expected to be less coherent than those examined here, resulting in smaller values of the correlation function. Oakley et al.[25] also reported measurements of $R_{u'u'}$ from their PIV measurements. The correlations that they measured had a tilted elliptical shape and also decayed faster than in the present experiment. However, as with Tung,[29] their measurements were also for a mixing layer that had undergone the mixing transition.

One significant difference between the correlation fields presented here and the measurements of Tung[29] is in spatial resolution. Whereas the spatial resolution of the present correlation fields consists of measurements at over 6400 locations, Tung's hot-wire measurements were made at less than 30 locations. This improved spatial resolution is essential for calculating linear stochastic estimates because the method used here to calculate those estimates requires differentiating the correlation fields. Thus, the greater spatial resolution of the present results reduces any errors introduced by differentiation.

The spatial correlation function $R_{v'v'}$ as measured by PIV is shown in Fig. 8. This correlation field is a vertically oriented ellipse. Once again, this is the expected shape considering the manner in which the mixing layer is dominated by rollers and braids; Fig. 3 can be used to demonstrate why this is so. Along the mixing-layer transverse centerline, the mean v velocity is nearly zero. However, moving along the same line in Fig. 3, great variation in the instantaneous value of v, that is, essentially v', is seen. It is this rapid variation in the corresponding v-velocity fluctuations that leads to short correlation distances in the x direction. Along a line of constant x, however, just the opposite is seen to be true; regardless of which line of constant x is chosen, there is little variation in the v-velocity fluctuation. This relative consistency of v-velocity fluctuations in the y direction leads to the long correlation distances in the y direction for the $R_{v'v'}$ correlation function.

Figure 8 also shows that, at x distances of approximately 1.2 vorticity thicknesses from the basis points, the correlation function becomes negatively correlated. The cause of this can be seen in Fig. 3. Consider the braid located at $x = 170$ mm. To the left of the braid is a large region where the velocity vectors all have negative v velocity. Similarly, there is a region to the right of the braid where the velocity vectors all have positive v velocity. These two regions, therefore, have negatively correlated v fluctuations. It is regions such as these that are responsible for the negatively correlated regions in the $R_{v'v'}$ correlation function.

The $R_{v'v'}$ correlation as measured in this experiment is found to be very similar to $R_{v'v'}$ as measured in the hot-wire experiment of Tung,[29] the major difference being that the correlation function measured by Tung is smaller than that measured in the present experiment. Once again, this is a result of the larger Reynolds number in Tung's experiment.

Finally, Fig. 9 is the spatial correlation function $R_{u'v'}$ as measured by PIV. Comparison of this correlation with the measurements of Tung[29] is not as easy as for the correlations discussed earlier. The two correlation functions are similar in that each has a peak value of 0.46 at the origin. However, Tung measured a correlation field that was approximately symmetrical about the origin, whereas the correlation field measured by PIV is not. The correlation contours in the PIV results of Fig. 9 suggest a tilted elliptical shape for the $R_{u'v'}$ correlation field, whereas the contours drawn by Tung from his hot-wire measurements at a limited number of spatial locations are more rectangular in shape. The correlation field measured by Tung was also found to decay more rapidly than in the present experiment, as is expected, considering once again the higher Reynolds number in the experiments of Tung.

Linear Stochastic Estimation

It is possible to calculate conditional velocity fields directly from the spatial correlations using linear stochastic estimation.[36,37] When

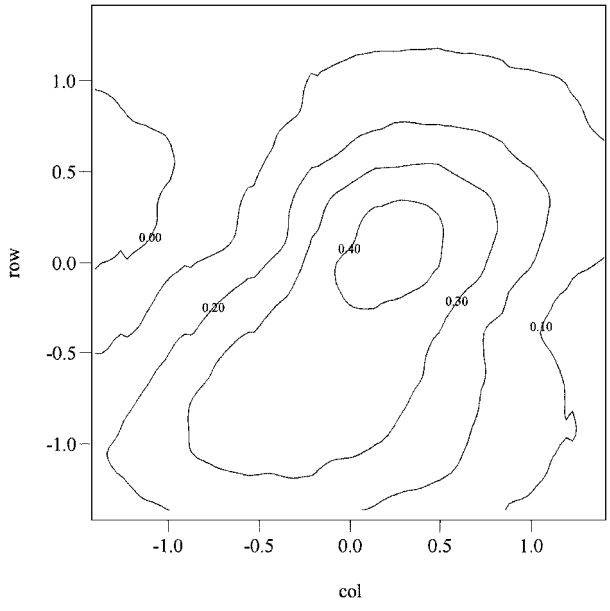

Fig. 9 Spatial correlation $R_{u'v'}$ as measured by PIV.

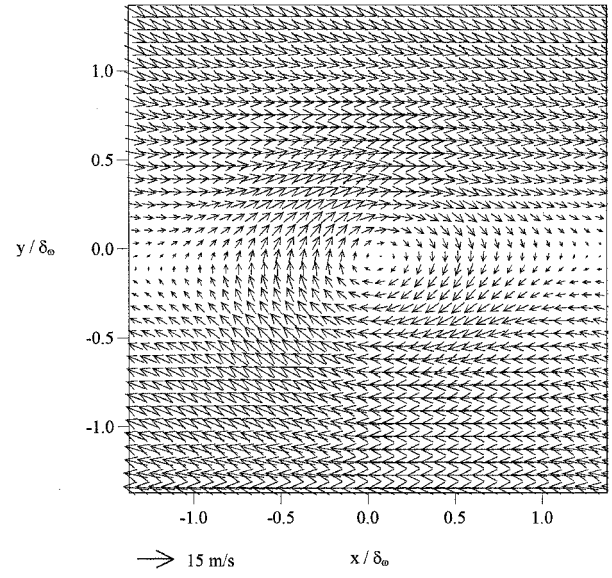

Fig. 10 Linear stochastic estimate of a roller structure.

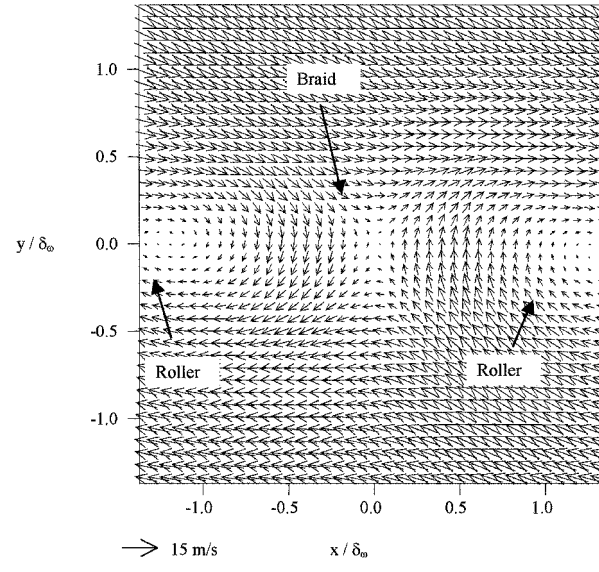

Fig. 11 Linear stochastic estimate of a braid.

the conditions corresponding to a specific large-scale structure are properly defined, the velocity field representing that structure based on the spatial correlations can be calculated. This was done for the present mixing layer by choosing conditions representative of both a roller structure and a braid.

Generally, a stochastic estimation is based on a velocity fluctuation at some location as the conditional event. Unfortunately, this type of estimate is not sufficient to obtain velocity fields for rollers and braids in mixing layers. At the center of a roller structure, the velocity fluctuations are zero, and at the center of a braid the velocity fluctuations are also zero, so that such an estimate will yield the same conditional velocity field for both a roller and a braid because the event on which both estimates are based will have been identical. Instead, a different conditional event is necessary to obtain stochastic estimates of roller and braid structures.

An investigation of instantaneous vorticity and shear strain fields revealed that rollers correspond to negative peaks in shear strain, and braids correspond to negative peaks in vorticity. It would, therefore, seem that a linear stochastic estimate for a mixing layer should incorporate this information. Thus, the linear stochastic estimates presented here are based on the local deformation at location x_0 and are given by

$$\langle u_i'(x)|d_{ij}(x_0)\rangle = A_i(x) + B_{ijk}(x)d_{jk}(x_0) \tag{4}$$

where d_{jk} is the deformation tensor. The coefficients $A_i(x)$ and $B_{ijk}(x)$ are then calculated by minimizing the mean square error of the estimate. This yields the result

$$A_i(x) = 0 \tag{5}$$

$$\langle u_{j,k}(x_0)u_{l,m}(x_0)\rangle B_{ijk}(x) = R_{u_l'u_{i,m}'} \tag{6}$$

which is a set of eight equations ($i, l, m = 1, 2$) that can be solved to obtain $B_{ijk}(x)$. Then, by the use of a given value for the deformation tensor at location x_0, Eq. (4) can be used to find the linear stochastic estimate of the velocity field.

First, several instantaneous vector fields were analyzed to find typical deformation tensor values at the centers of both roller structures and braids. These values were then used to calculate the linear stochastic estimates of rollers and braids for the mixing layer. The linear stochastic estimate for a roller structure is shown in Fig. 10. This estimate of a roller is seen to be very slightly elliptical with an approximately horizontal major axis. This shape is very similar to the roller structure shapes found by Moser and Rogers[21] in their DNSs. Also, braids can be seen to the left and right of the roller structure at about $x = \pm 1.3\delta_\omega$, which agrees well with the generally accepted value of $x = \pm 1.45\delta_\omega$ (Ref. 4). The linear stochastic estimate calculated here is expected to underestimate the average roller spacing slightly because the limited field of view of the PIV vector fields (done to obtain high spatial resolution) biases roller-structure spacing measurements toward smaller values.

Similarly, by the use of deformation tensor values typical of a braid structure, the linear stochastic estimate of a braid was calculated. The result is shown in Fig. 11. The braid can be seen at the center of the velocity vector field with roller structures to the right and left again centered at about $x = \pm 1.3\delta_\omega$. The linear stochastic estimate of the braid is obliquely oriented with stagnation occurring at a point. A similar braid shape was observed in the direct numerical simulations of Moser and Rogers[21] and also in the pulsed-laser inferomometry experiments of Meyer et al.[15]

The stochastic estimates prove valuable in comparing the sizes and shapes of large-scale structures in different experiments to determine the effects of varying such experimental parameters as Reynolds number and compressibility (convective Mach number), or in determining the effect of forcing on the structures. The stochastic estimate can be interpreted as depicting what a "typical" or "average" structure looks like in the flow, based in this case on the velocity field, and yields a more reliable comparison than comparing structures from individual realizations. To the authors' knowledge, this work represents the first stochastic estimates in a mixing layer based on the deformation tensor.

Conclusions

The incompressible mixing layer that was investigated was a homogeneous case ($s = \rho_2/\rho_1 = 1$) with a velocity ratio of $r = u_2/u_1 = 0.575$. Preliminary hot-film measurements indicated that 150 mm downstream of the tip of the splitter plate, the location where the PIV photographs were obtained, the mixing layer was self-similar in terms of the mean and fluctuating velocity profiles. At this location, $Re_x = 1.8 \times 10^5$, $Re_{\delta_\omega} = 1.1 \times 10^4$, and the pairing parameter was $Rx/\lambda = 8$.

An ensemble of 111 high-vector density PIV velocity fields was obtained for this mixing layer. The ensemble of velocity vector fields was used to calculate the ensemble-averaged mean velocity and Reynolds normal and shear stress profiles. To increase the number of realizations in the ensemble and, thus, yield more reliable statistics, the PIV data were condensed into a single column. The peak values of $\langle u' \rangle/\Delta U$, $\langle v' \rangle/\Delta U$, and $\langle u'v' \rangle/(\Delta U)^2$ were found to be 0.18, 0.16, and -0.010, respectively. These agree well with the results of previous hot-film experiments.

The planar velocity data were also used to calculate the spatial correlation fields of velocity fluctuations. The $R_{u'u'}$ correlation is elliptical, with the major axis slightly inclined to the horizontal (streamwise) direction; the $R_{v'v'}$ correlation is also an ellipse with a vertical (transverse) major axis. The $R_{u'v'}$ correlation is somewhat noisier than the other two correlations but appears to be elliptical and inclined to the streamwise direction with a peak value of 0.46 at the origin with lower values away from the origin. These correlations are similar in shape to those found by Tung[29] using hot-wire anemometry, with the major differences being that Tung's correlations were smaller in size and that the spatial resolution of the present results is far better. The difference in size of the correlation fields is easily explained by considering that Tung performed his experiments at a much higher Reynolds number than the present experiments. Thus, increasing Reynolds number appears to affect the size, but not the shape, of the correlation fields and, thus, the large-scale structures in incompressible mixing layers.

Finally, linear stochastic estimation was used to calculate conditional structures. The linear stochastic estimate was based on the deformation tensor, with typical values of the deformation tensor for rollers and braids used in the calculations. The linear stochastic estimate of a roller structure is very slightly elliptical with a horizontal major axis. The linear stochastic estimate of a braid was found to be oriented obliquely, with stagnation occurring at a point. Determining conditional velocity fields in a mixing layer is not a trivial task because of complications arising from the possibility that structures may be moving at different convective velocities. Because the linear stochastic estimates developed here based on the deformation tensor are not affected by this variation, however, they prove to be an effective technique for deducing conditional structure.

Acknowledgments

Support of this work was provided by the U.S. Army Research Office (Grant DAAG55-97-0122) with Thomas L. Doligalski as Monitor. The authors also thank Ronald J. Adrian for his help in formulating the linear stochastic estimation results and Terry Meyer for his assistance in collecting some of the hot-film results.

References

[1]Corrsin, S., and Kistler, A. L., "Free-Stream Boundaries of Turbulent Flows," NACA Rept. 1244, 1955.

[2]Townsend, A. A., "The Mechanism of Entrainment in Free Turbulent Flows," *Journal of Fluid Mechanics*, Vol. 26, 1966, pp. 689–715.

[3]Liepmann, H. W., and Laufer, J., "Investigation of Free Turbulent Mixing," NACA TN 1257, 1947.

[4]Brown, G. L., and Roshko, A., "On Density Effects and Large Structures in Turbulent Mixing Layers," *Journal of Fluid Mechanics*, Vol. 64, 1974, pp. 775–814.

[5]Roshko, A., "Structure of Turbulent Shear Flows: A New Look," *AIAA Journal*, Vol. 14, No. 10, 1976, pp. 1349–1357.

[6]Dimotakis, P. E., "Two-Dimensional Shear Layer Entrainment," *AIAA Journal*, Vol. 24, No. 11, 1986, pp. 1791–1796.

[7]Sato, H., "Experimental Investigation on the Transition of Laminar Separated Layer," *Journal of the Physical Society of Japan*, Vol. 11, No. 6, 1956, pp. 702–709.

[8]Sato, H., "Further Investigation on the Transition of Laminar Separated Layer," *Journal of the Physical Society of Japan*, Vol. 14, No. 12, 1959, pp. 1797–1810.

[9]Browand, F. K., and Weidman, P. D., "Large Scales in the Developing Mixing Layer," *Journal of Fluid Mechanics*, Vol. 76, 1976, pp. 127–144.

[10]Oster, D., and Wygnanski, I., "The Forced Mixing Layer Between Parallel Streams," *Journal of Fluid Mechanics*, Vol. 123, 1985, pp. 81–130.

[11]Ho, C. M., and Huang, L. S., "Subharmonics and Vortex Merging in Mixing Layers," *Journal of Fluid Mechanics*, Vol. 119, 1985, pp. 419–442.

[12]Winant, C. D., and Browand, F. K., "Vortex Pairing: the Mechanism of Turbulent Mixing Layer Growth at Moderate Reynolds Number," *Journal of Fluid Mechanics*, Vol. 63, 1974, pp. 237–255.

[13]Karasso, P. S., and Mungal, M. G., "Scalar Mixing and Reaction in Plane Liquid Shear Layers," *Journal of Fluid Mechanics*, Vol. 323, 1996, pp. 23–63.

[14]Huang, L. S., and Ho, C. M., "Small-Scale Transition in Plane Mixing Layer," *Journal of Fluid Mechanics*, Vol. 210, 1990, pp. 475–500.

[15]Meyer, T. R., Dutton, J. C., and Lucht, R. P., "Vortex Interaction and Mixing in a Driven Gaseous Axisymmetric Jet," *Physics of Fluids*, Vol. 11, No. 11, 1999, pp. 3401–3415.

[16]Bernal, L. P., and Roshko, A., "Streamwise Vortex Structure in Plane Mixing Layers," *Journal of Fluid Mechanics*, Vol. 170, 1986, pp. 499–525.

[17]Breidenthal, R., "Structure in Turbulent Mixing Layers and Wakes Using a Chemical Reaction," *Journal of Fluid Mechanics*, Vol. 109, 1981, pp. 1–24.

[18]Tung, S., and Kleis, S. J., "Initial Streamwise Vorticity Formation in a Two-Stream Mixing Layer," *Journal of Fluid Mechanics*, Vol. 319, 1996, pp. 251–279.

[19]Metcalfe, R. W., Hussain, A. K. M. F., Menon, S., and Hayakawa, M., "Coherent Structures in a Turbulent Mixing Layer: A Comparison Between Direct Numerical Simulations and Experiments," *Turbulent Shear Flows 5*, Springer-Verlag, Berlin, 1987, pp. 110–122.

[20]Moser, R. D., and Rogers, M. M., "Mixing Transition and the Cascade to Small Scales in a Plane Mixing Layer," *Physics of Fluids*, Vol. 3, No. 5, 1991, pp. 1128–1134.

[21]Moser, R. D., and Rogers, M. M., "The Three-Dimensional Evolution of a Plane Mixing Layer: Pairing and Transition to Turbulence," *Journal of Fluid Mechanics*, Vol. 247, 1993, pp. 275–320.

[22]Rogers, M. M., and Moser, R. D., "Direct Numerical Simulation of a Self-Similar Turbulent Mixing Layer," *Physics of Fluids*, Vol. 6, No. 2, 1994, pp. 903–923.

[23]Dimotakis, P. E., Debussy, F. D., and Koochesfahani, M. M., "Particle Streak Velocity Field Measurements in a Two-Dimensional Mixing Layer," *Physics of Fluids*, Vol. 24, 1981, pp. 995–999.

[24]Post, M. E., Trump, D. D., Goss, L. P., and Hancock, R. D., "Two-Color Particle Image Velocimetry Using a Single Argon-Ion Laser," *Experiments in Fluids*, Vol. 16, No. 3/4, 1994, pp. 263–272.

[25]Oakley, T. R., Loth, E., and Adrian, R. J., "Cinematic Particle Image Velocimetry of High-Reynolds-Number Turbulent Free Shear Layer," *AIAA Journal*, Vol. 34, No. 2, 1996, pp. 299–308.

[26]Samimy, M., and Lele, S. K., "Motion of Particles with Inertia in a Compressible Free Shear Layer," *Physics of Fluids A*, Vol. 3, No. 8, 1991, pp. 1915–1923.

[27]Prasad, A. K., Adrian, R. J., Landreth, C. C., and Offutt, P. W., "Effect of Resolution on the Speed and Accuracy of Particle Image Velocimetry Interrogation," *Experiments in Fluids*, Vol. 13, No. 2/3, 1992, pp. 105–116.

[28]Schlichting, H., *Boundary Layer Theory*, 6th ed., McGraw–Hill, New York, 1968, pp. 689, 690.

[29]Tung, A. T.-C., "Properties of Conditional Eddies in Free Shear Flows," Ph.D. Dissertation, Dept. of Theoretical and Applied Mechanics, Univ. of Illinois, Urbana, IL, 1982.

[30]Spencer, B. W., "Statistical Investigation of Turbulent Velocity and Pressure Fields in a Two-Stream Mixing Layer," Ph.D. Dissertation, Dept. of Nuclear Engineering, Univ. of Illinois, Urbana, IL, 1970.

[31]Batt, R. G., "Some Measurements of the Effect of Tripping the Two-Dimensional Shear Layer," *AIAA Journal*, Vol. 13, No. 2, 1975, pp. 245–247.

[32]Wygnanski, I., and Fiedler, H. E., "The Two-Dimensional Mixing Region," *Journal of Fluid Mechanics*, Vol. 41, 1970, pp. 327–361.

[33]Browand, F. K., and Latigo, B. O., "Growth of the Two-Dimensional Mixing Layer from a Turbulent and Nonturbulent Boundary Layer," *Physics of Fluids*, Vol. 22, No. 6, 1979, pp. 1011–1019.

[34]Urban, W. D., and Mungal, M. G., "Planar Velocity Measurements in Compressible Mixing Layers," *Journal of Fluid Mechanics*, Vol. 431, 2001, pp. 189–222.

[35]Dziomba, B., and Fiedler, H. E., "Effect of Initial Conditions on Two-Dimensional Free Shear Layers," *Journal of Fluid Mechanics*, Vol. 152, 1985, pp. 419–442.

[36]Adrian, R. J., Jones, B. G., Chung, M. K., Nithianandan, C. K., and Tung, A. T.-C., "Approximation of Turbulent Conditional Averages by Stochastic Estimation," *Physics of Fluids A*, Vol. 1, No. 6, 1989, pp. 992–996.

[37]Adrian, R. J., "Stochastic Estimation of Conditional Structure: A Review," *Applied Scientific Research*, Vol. 53, No. 3/4, 1994, pp. 291–303.

P. Givi
Associate Editor